A *k*-space method for coupled first-order acoustic propagation equations

Makoto Tabei
Department of Electrical and Computer Engineering, University of Rochester, Rochester, New York 14627

T. Douglas Mast
Applied Research Laboratory, The Pennsylvania State University, University Park, Pennsylvania 16801

Robert C. Waag
Departments of Electrical and Computer Engineering and Radiology, University of Rochester, Rochester, New York 14627

(Received 11 June 2001; accepted for publication 8 October 2001)

A *k*-space method for large-scale simulation of ultrasonic pulse propagation is presented. The present method, which solves the coupled first-order differential equations for wave propagation in inhomogeneous media, is derived in a simple form analogous to previous finite-difference methods with staggered spatial and temporal grids. Like *k*-space methods based on second-order wave equations, the present method is exact for homogeneous media, unconditionally stable for ''slow'' $[c(\mathbf{r}) \leqslant c_0]$ media, and highly accurate for general weakly scattering media. In addition, unlike previous *k*-space methods, the form of the method allows straightforward inclusion of relaxation absorption and perfectly matched layer (PML) nonreflecting boundary conditions. Numerical examples illustrate the capabilities of the present *k*-space method. For weakly inhomogeneous media, accurate results are obtained using coarser temporal and spatial steps than possible with comparable finite-difference and pseudospectral methods. The low dispersion of the *k*-space method allows accurate representation of frequency-dependent attenuation and phase velocity associated with relaxation absorption. A technique for reduction of Gibbs phenomenon artifacts, in which compressibility and exponentially scaled density functions are smoothed by half-band filtering, is introduced. When employed together with this smoothing technique, the *k*-space method provides high accuracy for media including discontinuities, high-contrast inhomogeneities, and scattering structures smaller than the spatial grid resolution. © *2002 Acoustical Society of America.*
[DOI: [10.1121/1.1421344]

PACS numbers: 43.20.Fn, 43.80.Qf, 43.35.Fj [ADP]

I. INTRODUCTION

This paper presents a method for computation of acoustic propagation in inhomogeneous media. The present method is an adaptation of the *k*-space method originally derived by Bojarski[1,2] and extended by several others.[3–5] As shown in Ref. 6, the *k*-space method has considerable advantages for large-scale simulations of ultrasonic propagation in soft tissues. The *k*-space method combines accurate spectral evaluation of spatial derivatives with a temporal iteration procedure that is exact for homogeneous media. For soft tissues, in which local medium properties show small variations around nominal background properties, this method provides excellent efficiency and accuracy compared to other approaches such as finite-difference and pseudospectral methods.[6,7]

Previous formulations of the *k*-space method for acoustic propagation have numerically solved second-order differential wave equations. Such formulations have some advantages, including conceptual simplicity and computational efficiency, since the acoustic fields are defined by only one independent variable, the acoustic pressure fluctuation, instead of acoustic pressure and vector particle velocity fluctuations. Propagation in inhomogeneous media including density variations can be computed using a simple transformation of the pressure variable (e.g., as in Refs. 5 and 6).

However, several desirable extensions to the *k*-space method are not possible using the usual second-order formulation. In particular, perfectly matched layer (PML) absorbing boundary conditions are not readily incorporated into current second-order *k*-space methods, while PMLs are easily formulated for coupled first-order acoustic propagation equations. Additionally, as derived in Ref. 8, the full wave equation incorporating relaxation absorption effects is of order $2+N$, where N is the number of relaxation processes employed. Relaxation effects can be incorporated more simply into numerical methods using coupled first-order acoustic propagation equations.[9]

Here, a *k*-space method is derived based on the coupled first-order differential equations for linear acoustic propagation. The method accounts for spatially varying sound speed, density, and relaxation absorption processes, and includes PML absorbing boundary conditions. The formulation of this method shows that the *k*-space method can be regarded as a finite-difference method containing linear correction operators. Use of staggered spatial and temporal grids increases the range of applicability for the method, and facilitates inclusion of relaxation absorption and PML boundary conditions. The close analogy between the method presented here

and existing finite-difference methods allows extensions developed for finite-difference methods to be easily applied to the *k*-space method, and also allows current finite-difference algorithms to be improved by inclusion of the *k*-space operators introduced here.

The present *k*-space method is, like previous *k*-space methods based on second-order wave equations,[6] temporally exact for homogeneous media. For general media, the present method also has accuracy and efficiency advantages similar to previous *k*-space methods. Numerical results presented here show that the *k*-space method presented here has the high accuracy and stability characteristics of the original *k*-space method, including unconditional stability for media with $c(\mathbf{r}) \leqslant c_0$. The low numerical dispersion inherent to the *k*-space method allows the frequency-dependent absorption and physical dispersion associated with relaxation-process absorption to be accurately modeled.

A method for smoothing of discontinuous scattering media is also presented here. Together with the *k*-space method, this smoothing method is shown to provide accurate results for strongly scattering media and for media with structures smaller than the grid resolution. Numerical examples also demonstrate the efficiency of the present *k*-space method for large-scale computations of interest in ultrasonic imaging studies.

II. THEORY

A. Second-order and first-order *k*-space methods

The *k*-space method derived below is based on the coupled first-order linear acoustic propagation equations for a fluid medium of variable sound speed and density. For a lossless two-dimensional medium, these are[10]

$$\begin{aligned} \rho(\mathbf{r}) \frac{\partial \mathbf{u}(\mathbf{r},t)}{\partial t} &= -\nabla p(\mathbf{r},t) \\ \frac{1}{\rho(\mathbf{r})\, c(\mathbf{r})^2} \frac{\partial p(\mathbf{r},t)}{\partial t} &= -\nabla \cdot \mathbf{u}(\mathbf{r},t), \end{aligned} \tag{1}$$

where $\mathbf{u}$ is the (vector) acoustic particle velocity fluctuation with components u_x and u_y, p is the acoustic pressure fluctuation, $\rho(\mathbf{r})$ is the density of the medium, $c(\mathbf{r})$ is the sound speed of the medium, and $\mathbf{r}$ denotes the vector coordinate (x,y).

Many numerical methods for acoustic wave propagation have been based on Eq. (1). For example, in Ref. 11, ultrasonic propagation in an abdominal model was computed using a finite-difference method applied directly to the coupled equations.

The second-order wave equation corresponding to Eq. (1) is[10]

$$\nabla \cdot \left(\frac{1}{\rho(\mathbf{r})} \nabla p(\mathbf{r},t) \right) - \frac{1}{\rho(\mathbf{r})\, c(\mathbf{r})^2} \frac{\partial^2 p(\mathbf{r},t)}{\partial t^2} = 0. \tag{2}$$

This equation can be solved numerically by the *k*-space method. Below, a brief sketch of the *k*-space solution to Eq. (2) will be given and this solution will be analyzed to obtain a corresponding *k*-space method for coupled first-order propagation equations. For simplicity, the derivation will assume sound speed and density are constant, i.e., $\rho(\mathbf{r}) = \rho_0$ and $c(\mathbf{r}) = c_0$. A general derivation of the second-order *k*-space method is given in Ref. 6, while the first-order *k*-space method is straightforwardly extended to inhomogeneous media, as seen below.

For bandlimited signals such as typical ultrasonic pulses, very accurate spatial derivatives can be obtained by Fourier transformation of the pressure field.[12] This is the principle behind pseudospectral methods like that described in Ref. 13, in which the spatial derivatives from Eq. (1) are evaluated using discrete Fourier transformation and temporal iteration is performed using a fourth-order Adams–Bashforth/Adams–Moulton scheme. For the case of homogeneous sound speed and density, Eq. (2) can be written in the spatial-frequency domain as

$$\frac{\partial^2 \hat{p}(\mathbf{k},t)}{\partial t^2} = -c_0^2 k^2 \hat{p}(\mathbf{k},t), \tag{3}$$

where $\hat{p}(\mathbf{k},t)$ is the two-dimensional spatial Fourier transform of the acoustic pressure fluctuation $p(\mathbf{r},t)$.

A discrete form of the left-hand side of Eq. (3), obtained using a second-order-accurate finite-difference scheme, yields a crude pseudospectral method, expressed as

$$\begin{aligned} &\frac{p(\mathbf{r},t+\Delta t) - 2p(\mathbf{r},t) + p(\mathbf{r},t-\Delta t)}{(\Delta t)^2} \\ &\quad = -c_0^2\, \mathbf{F}^{-1}[k^2\, \mathbf{F}[p(\mathbf{r},t)]], \end{aligned} \tag{4}$$

where $\mathbf{F}$ represents the two-dimensional spatial Fourier transform. In numerical implementations of Eq. (4), the spatial derivatives from the right-hand side of Eq. (3) are accurately represented using discrete Fourier transformation. Still, the discrete representation of the temporal derivative on the left-hand side is significantly dispersive. Current pseudospectral methods[12,13] typically use higher-order temporal integration schemes to decrease dispersion errors. However, for the homogeneous-medium case, temporal iteration can be performed exactly (e.g., without any dispersion) using the $k-t$ space scheme[6]

$$\frac{\hat{p}(\mathbf{k},t+\Delta t) - 2\,\hat{p}(\mathbf{k},t) + \hat{p}(\mathbf{k},t-\Delta t)}{(\Delta t)^2\, \mathrm{sinc}(c_0 \Delta t\, k/2)^2} = -(c_0 k)^2 \hat{p}(\mathbf{k},t), \tag{5}$$

where $\mathrm{sinc}(\mu) \equiv \sin(\mu)/(\mu)$. The temporal iteration scheme of Eq. (5) is mathematically equivalent to the scheme originally presented in Ref. 2. (A similar exact discretization for the linear part of the Korteweg–de Vries equation was presented in Ref. 14.)

As discussed in Ref. 6, the temporal exactness of this scheme follows from an exact discrete representation of the harmonic-oscillator differential equation, described in Ref. 15. Temporal iteration can be performed in the spatial-frequency domain, as done in Ref. 6 using a generalized form of Eq. (5). Alternatively, an equivalent iteration method employing the real-space pressure can be obtained by inverse spatial Fourier transformation of Eq. (5). The resulting iteration formula is

$$\frac{p(\mathbf{r},t+\Delta t)-2\,p(\mathbf{r},t)+p(\mathbf{r},t-\Delta t)}{(\Delta t)^2}$$
$$=-c_0^2\,\mathbf{F}^{-1}[k^2\,\mathrm{sinc}(c_0\Delta t\,k/2)^2\,\mathbf{F}[p(\mathbf{r},t)]]. \tag{6}$$

Below, the operation on the right-hand side of Eq. (6) is called the second-order k-space operator. This operator is defined as

$$[\nabla^{(c_0\Delta t)}]^2 p(\mathbf{r},t)\equiv-\mathbf{F}^{-1}[k^2\,\mathrm{sinc}(c_0\Delta t\,k/2)^2\mathbf{F}[p(\mathbf{r},t)]]; \tag{7}$$

the $(c_0\Delta t)$ superscript is meant to signify that the operators employed, while similar to the standard gradient operator, are also functions of the parameter $c_0\Delta t$.

The form of Eq. (6) suggests that the second-order k-space method can be considered a corrected finite-difference method in which the spatial Laplacian is replaced by the k-space operator. However, the k-space operator of Eq. (7) incorporates not only spectral evaluation of the Laplacian, but also a temporal correction term associated with the $k-t$ space iterator of Eq. (5).

To construct a k-space method for coupled first-order wave propagation equations, the second-order k-space operator can be factored into parts associated with each spatial direction. Below, this procedure is carried out for the two-dimensional case. An appropriate factorization is given by the first-order k-space operators

$$\begin{aligned}
\frac{\partial p(\mathbf{r},t)}{\partial^{(c_0\Delta t)^+}x}&\equiv\mathbf{F}^{-1}[ik_x\,e^{ik_x\Delta_x/2}\,\mathrm{sinc}(c_0\Delta t\,k/2)\mathbf{F}[p(\mathbf{r},t)]],\\
\frac{\partial p(\mathbf{r},t)}{\partial^{(c_0\Delta t)^+}y}&\equiv\mathbf{F}^{-1}[ik_y\,e^{ik_y\Delta_y/2}\,\mathrm{sinc}(c_0\Delta t\,k/2)\mathbf{F}[p(\mathbf{r},t)]],\\
\frac{\partial p(\mathbf{r},t)}{\partial^{(c_0\Delta t)^-}x}&\equiv\mathbf{F}^{-1}[ik_x\,e^{-ik_x\Delta_x/2}\,\mathrm{sinc}(c_0\Delta t\,k/2)\mathbf{F}[p(\mathbf{r},t)]],\\
\frac{\partial p(\mathbf{r},t)}{\partial^{(c_0\Delta t)^-}y}&\equiv\mathbf{F}^{-1}[ik_y\,e^{-ik_y\Delta_y/2}\,\mathrm{sinc}(c_0\Delta t\,k/2)\mathbf{F}[p(\mathbf{r},t)]],
\end{aligned} \tag{8}$$

so that

$$\left(\frac{\partial}{\partial^{(c_0\Delta t)^+}x}\frac{\partial}{\partial^{(c_0\Delta t)^-}x}+\frac{\partial}{\partial^{(c_0\Delta t)^+}y}\frac{\partial}{\partial^{(c_0\Delta t)^-}y}\right)p(\mathbf{r},t)$$
$$=[\nabla^{(c_0\Delta t)}]^2 p(\mathbf{r},t). \tag{9}$$

The spatial-frequency components k_x and k_y are defined such that $k^2=k_x^2+k_y^2$.

Using the operators of Eq. (8) within Eq. (1) enables construction of a first-order k-space method equivalent to Eq. (6). Application of the exponential coefficients from Eq. (8) requires the acoustic particle velocity variables u_x and u_y to be evaluated on grid points staggered by distances of $\Delta x/2$ and $\Delta y/2$, respectively. The resulting algorithm is

$$\begin{aligned}
\frac{u_x(\mathbf{r}_1,t^+)-u_x(\mathbf{r}_1,t^-)}{\Delta t}&=-\frac{1}{\rho(\mathbf{r}_1)}\frac{\partial p(\mathbf{r},t)}{\partial^{(c_0\Delta t)^+}x},\\
\frac{u_y(\mathbf{r}_2,t^+)-u_y(\mathbf{r}_2,t^-)}{\Delta t}&=-\frac{1}{\rho(\mathbf{r}_2)}\frac{\partial p(\mathbf{r},t)}{\partial^{(c_0\Delta t)^+}y},
\end{aligned} \tag{10}$$

$$\frac{p(\mathbf{r},t+\Delta t)-p(\mathbf{r},t)}{\Delta t}=-\rho(\mathbf{r})\,c(\mathbf{r})^2\left(\frac{\partial u_x(\mathbf{r}_1,t^+)}{\partial^{(c_0\Delta t)^-}x}+\frac{\partial u_y(\mathbf{r}_2,t^+)}{\partial^{(c_0\Delta t)^-}y}\right),$$

where

$$\begin{aligned}
&\mathbf{r}_1\equiv(x+\Delta x/2,y),\quad \mathbf{r}_2\equiv(x,y+\Delta y/2),\\
&t^+\equiv t+\Delta t/2,\ \text{and}\ \ t^-\equiv t-\Delta t/2.
\end{aligned} \tag{11}$$

In Eq. (10), the coefficients c_0 and ρ_0 have been replaced by the spatially varying sound speed and density $c(\mathbf{r})$ and $\rho(\mathbf{r})$. Spatial staggering in Eq. (10) is implicitly incorporated into the spatial derivative operators employed. For example, the operators $\partial/\partial^{(c_0\Delta t)^+}x$ and $\partial/\partial^{(c_0\Delta t)^-}x$ defined by Eq. (8) correspond, by the shift property of Fourier transformation, to derivatives evaluated after spatial shifts of $\Delta x/2$ and $-\Delta x/2$, respectively.

Staggered temporal grids, discussed in the following section, have also been employed in Eq. (10). Notable is that the ordering of $(c_0\Delta t)^+$ and $(c_0\Delta t)^-$ operators is arbitrary depending on how the staggered grids are configured; however, for solution of coupled equations, the operators should be used in pairs such that the spatial shifting operations cancel out over any temporal interval of length Δt. Rationale for the use of spatial and temporal staggering is given in the following section.

The k-space method of Eq. (10) is straightforwardly shown to be equivalent to Eq. (5) for $c(\mathbf{r})=c_0$ and $\rho(\mathbf{r})=\rho_0$. Thus, this first-order k-space scheme is temporally exact for homogeneous media. As shown below, the method also provides high accuracy for media with properties are close to the background values, and in conjunction with an appropriate smoothing algorithm, yields high accuracy even for media including high-contrast discontinuities.

Theoretical stability limits for the present k-space method can be computed as described in Ref. 6; given neglect of density variations and assumption of a worst-case sound-speed variation $c(\mathbf{r})=c_{\max}$, the results are identical to those for the second-order k-space method. The resulting theoretical stability boundary is

$$\sin\frac{\pi\,\mathrm{CFL}}{2}\leqslant\frac{c_0}{c_{\max}}, \tag{12}$$

where CFL denotes the Courant–Friedrichs–Lewy number $c_0\Delta t/\Delta x$. Thus, like the original k-space method,[6] the k-space method derived above is also expected to be unconditionally stable for media with $c(\mathbf{r})\leqslant c_0$ everywhere.

As with the second-order k-space method, the first-order method of Eq. (10) can be regarded as a finite-difference method with correction factors that appear within the spatial derivative terms. The k-space algorithm of Eq. (10) is analogous to standard second-order-accurate finite-difference methods for computation of acoustic wave propagation[9,16] except that second-order-accurate spatial derivatives have been replaced by the k-space operators of Eq. (8) that incorporate spectral spatial accuracy as well as corrected temporal iteration.

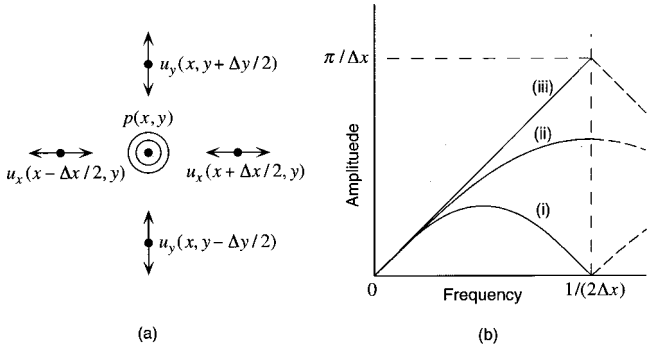

FIG. 1. Characteristics of discrete spatial derivative operators. (a) Sampling locations for spatially staggered grid. (b) Spatial-frequency response of first-derivative operators: (i) nonstaggered grid; (ii) staggered grid; (iii) ideal.

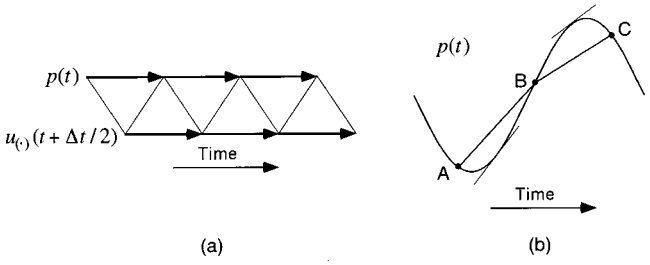

FIG. 2. Characteristics of discrete time derivative operators. (a) Time-staggered sampling for acoustic pressure and particle velocity. (b) Derivatives estimated using a staggered time scheme and true derivatives evaluated at the center of the time step.

B. Properties of staggered spatial and temporal grids

The temporal and spatial sampling configuration employed in the *k*-space method of Eq. (10) is directly analogous to staggered-space, staggered-time schemes employed in previous finite-difference methods.[9,16] Such staggered configurations are known to increase accuracy and stability for discrete representations of odd-order spatial and temporal derivatives.[12] For example, because the discrete Fourier transform is implicitly periodic, Gibbs phenomenon (ringing) artifacts result if the coefficients on the right-hand side of Eq. (8) have different values at the maximum spatial frequency $\pi/\Delta x$ and the minimum negative spatial frequency $-\pi/\Delta x$. The coefficient ik (which would correspond to a nonstaggered spatial grid) has a jump discontinuity of magnitude $2\pi/\Delta x$ at the transition between $k=\pi/\Delta x$ and $k=-\pi/\Delta x$. Coefficients of the form used in Eqs. (8) remove this discontinuity and, thus, can substantially reduce numerical artifacts in some cases, such as when the wave field is spatially undersampled. Accuracy and stability are particularly increased for media containing large discontinuities.[17]

Although staggering slightly increases the complexity of the *k*-space algorithm, the benefit from spatial staggering can be easily understood by examining the physical relationship between sound pressure and particle velocity. Figure 1(a) represents the spatial sampling locations for sound pressure and particle velocity in the present staggered grid. The arrow at each sampling location indicates the direction of particle motion represented by each parameter. In this configuration, a local change in sound pressure $p(x,y)$ immediately affects the adjacent particle velocities. On the contrary, in a nonstaggered grid configuration, in which p, u_x, and u_y are all sampled at the same grid points, symmetry prohibits a local change in sound pressure from immediately affecting the particle velocity components sampled at the same position. This effect limits the accuracy of computations for high-spatial-frequency components of the wave field.

Figure 1(b) shows the spatial-frequency response of the second-order-accurate discrete finite-difference operators for the first-order spatial derivative. Curve (i) shows the response for a nonstaggered center difference configuration, curve (ii) shows the corresponding response for the staggered grid center difference configuration, and curve (iii) shows the ideal frequency response for the continuous first-order derivative. Finite-difference schemes with higher-order accuracy show improved high-spatial-frequency response. Spectral computation of the first derivative on a staggered spatial grid, performed implicitly within the present *k*-space method, achieves this ideal frequency response up to the spatial Nyquist frequency $\pi/\Delta x$.

Figure 2 illustrates the characteristics of the temporal scheme employed. In panel (a), the temporal iteration process is shown for the staggered-time marching scheme. Because the time step is interleaved, time derivatives are evaluated based on values of spatial derivatives at the center of each time step. This staggering minimizes error when a crude time integration (Euler) scheme is employed. Panel (b) shows the difference between true derivatives (slopes of the tangential lines) and staggered finite differences (slopes of the straight lines between A, B, and C) at the center of each time step. Although time staggering reduces the error between the finite difference and the actual derivative, staggered finite-difference schemes still incur significant error with large time steps. This error is compensated in the *k*-space method by introducing a correction factor that leads to a temporally exact solution for a medium with constant sound speed. Although a temporally exact discrete solution can also be obtained using a nonstaggered grid,[15] staggered grids allow the necessary compensation to be performed using a single multiplicative factor. Use of a staggered time scheme also facilitates modeling of absorption, as shown in the next section. Thus, temporal staggering is important to the first-order *k*-space method.

C. Relaxation absorption and perfectly matched layers

The close analogy between the *k*-space method of Eq. (10) and standard finite-difference techniques[16] allows easy addition of features such as perfectly matched layer (PML) absorbing boundary conditions and relaxation-process absorption to the present *k*-space method.

In the following, the acoustic pressure fluctuation $p(\mathbf{r},t)$ is split into x and y components, $p(\mathbf{r},t)=p_x(\mathbf{r},t)+p_y(\mathbf{r},t)$. This splitting allows definition of direction-dependent absorption, which is necessary for incorporation of the PML.[9] Following the procedure applied to the finite-difference method in Ref. 9, the field equations are then written as a group of coupled first-order equations, with decay terms corresponding to relaxation absorbtion and to the PML. Discrete

forms of these field equations are defined in a manner that provides high accuracy in the presence of large absorption.[9]

The (continuous) field equations for a PML medium with relaxation absorption can be written as

$$\rho(\mathbf{r})\left(\frac{\partial u_x(\mathbf{r},t)}{\partial t}+\alpha_x(\mathbf{r})\,u_x(\mathbf{r},t)\right)=-\frac{\partial(p_x(\mathbf{r},t)+p_y(\mathbf{r},t))}{\partial x}, \tag{13}$$

$$\rho(\mathbf{r})\left(\frac{\partial u_y(\mathbf{r},t)}{\partial t}+\alpha_y(\mathbf{r})\,u_y(\mathbf{r},t)\right)=-\frac{\partial(p_x(\mathbf{r},t)+p_y(\mathbf{r},t))}{\partial y}, \tag{14}$$

$$\kappa(\mathbf{r},t)\otimes\left(\frac{\partial p_x(\mathbf{r},t)}{\partial t}+\alpha_x(\mathbf{r})\,p_x(\mathbf{r},t)\right)=-\frac{\partial u_x(\mathbf{r},t)}{\partial x}, \tag{15}$$

$$\kappa(\mathbf{r},t)\otimes\left(\frac{\partial p_y(\mathbf{r},t)}{\partial t}+\alpha_y(\mathbf{r})\,p_y(\mathbf{r},t)\right)=-\frac{\partial u_y(\mathbf{r},t)}{\partial y}, \tag{16}$$

where $\alpha_x(\mathbf{r})$ and $\alpha_y(\mathbf{r})$ are dispersionless absorption parameters employed only within the PML and the $\otimes$ operator denotes temporal convolution. Equations (15) and (16) contain a generalized compressibility,[8] defined as

$$\kappa(\mathbf{r},t)\equiv\kappa_\infty(\mathbf{r})\,\delta(t)+\sum_{i=1}^{N}\frac{\kappa_i(\mathbf{r})}{\tau_i(\mathbf{r})}e^{-t/\tau_i(\mathbf{r})}H(t), \tag{17}$$

where $\kappa_\infty(\mathbf{r})$ is the usual compressibility $1/[\rho(\mathbf{r})c(\mathbf{r})^2]$, $\tau_i(\mathbf{r})$ is the relaxation time for the ith relaxation process, $\kappa_i(\mathbf{r})$ is the relaxation modulus for the ith-order relaxation process, with units of compressibility, and $H(t)$ is the Heaviside step function. The integration (convolution) terms in Eqs. (15) and (16) make these equations equivalent to second-order differential equations in time. The convolution terms can be simplified using properties of the Dirac δ function and Heaviside step function that appear in the generalized compressibility (17) as well as identities for convolutions involving time derivatives.[9] Thus, for example, the left-hand side of Eq. (15) can be written as

$$\begin{aligned}&\kappa_\infty(\mathbf{r})\left(\frac{\partial p_x(\mathbf{r},t)}{\partial t}+\alpha_x(\mathbf{r})\,p_x(\mathbf{r},t)\right)+\sum_{i=1}^{N}\frac{\kappa_i(\mathbf{r})}{\tau_i(\mathbf{r})}p_x(\mathbf{r},t)\\&\quad+\left[\sum_{i=1}^{N}\frac{\kappa_i(\mathbf{r})}{\tau_i(\mathbf{r})}e^{-t/\tau_i(\mathbf{r})}H(t)\left(-\frac{1}{\tau_i(\mathbf{r})}+\alpha_x(\mathbf{r})\right)\right]\\&\quad\otimes p_x(\mathbf{r},t).\end{aligned}$$

The last term in this latter expression is still a convolution of two time-dependent functions, and this form presents difficulties for numerical implementation. The difficulties can be resolved by introducing a state variable, which allows Eqs. (13)–(16) to be rewritten as a set of simultaneous first-order differential equations. The state variable employed here is a filtered version of the acoustic pressure fluctuation, defined as

$$S_i^{(\cdot)}(\mathbf{r},t)\equiv\left(\frac{e^{-t/\tau_i(\mathbf{r})}}{\tau_i(\mathbf{r})}H(t)\right)\otimes p_{(\cdot)}(\mathbf{r},t), \tag{18}$$

where $(\cdot)$ denotes x or y.

Using the state variables defined by Eq. (18), the continuous field equations are rewritten as the coupled first-order differential equations

$$\begin{aligned}&\frac{\partial u_x(\mathbf{r},t)}{\partial t}+\alpha_x(\mathbf{r})\,u_x(\mathbf{r},t)=-\frac{1}{\rho(\mathbf{r})}\frac{\partial(p_x(\mathbf{r},t)+p_y(\mathbf{r},t))}{\partial x},\\&\frac{\partial u_y(\mathbf{r},t)}{\partial t}+\alpha_y(\mathbf{r})\,u_y(\mathbf{r},t)=-\frac{1}{\rho(\mathbf{r})}\frac{\partial(p_x(\mathbf{r},t)+p_y(\mathbf{r},t))}{\partial y},\\&\frac{\partial p_x(\mathbf{r},t)}{\partial t}+\mu_x(\mathbf{r})\,p_x(\mathbf{r},t)\\&\quad=-\frac{1}{\kappa_\infty(\mathbf{r})}\left[\frac{\partial u_x(\mathbf{r},t)}{\partial x}-\sum_{i=1}^{N}\nu_i^x(\mathbf{r})\,S_i^x(\mathbf{r},t)\right],\\&\frac{\partial p_y(\mathbf{r},t)}{\partial t}+\mu_y(\mathbf{r})\,p_y(\mathbf{r},t)\\&=-\frac{1}{\kappa_\infty(\mathbf{r})}\left[\frac{\partial u_y(\mathbf{r},t)}{\partial y}-\sum_{i=1}^{N}\nu_i^y(\mathbf{r})S_i^y(\mathbf{r},t)\right],\\&\frac{\partial S_i^x(\mathbf{r},t)}{\partial t}+\frac{1}{\tau_i(\mathbf{r})}S_i^x(\mathbf{r},t)=\frac{p_x(\mathbf{r},t)}{\tau_i(\mathbf{r})},\\&\frac{\partial S_i^y(\mathbf{r},t)}{\partial t}+\frac{1}{\tau_i(\mathbf{r})}S_i^y(\mathbf{r},t)=\frac{p_y(\mathbf{r},t)}{\tau_i(\mathbf{r})},\end{aligned} \tag{19}$$

where

$$\mu_{(\cdot)}(\mathbf{r})\equiv\frac{1}{\kappa_\infty(\mathbf{r})}\sum_{i=1}^{N}\frac{\kappa_i(\mathbf{r})}{\tau_i(\mathbf{r})}+\alpha_{(\cdot)}(\mathbf{r}), \tag{20}$$

and

$$\nu_i^{(\cdot)}(\mathbf{r})\equiv\frac{\kappa_i(\mathbf{r})}{\tau_i(\mathbf{r})}-\kappa_i(\mathbf{r})\,\alpha_{(\cdot)}(\mathbf{r}). \tag{21}$$

Each of Eqs. (19) has the form

$$\frac{\partial R(\mathbf{r},t)}{\partial t}+\beta R(\mathbf{r},t)=Q(\mathbf{r},t), \tag{22}$$

where β is a constant that controls the decay of a field variable R. Following Ref. 9, the field equations can be transformed into a form that allows larger attenuations without numerical instability. This form is

$$\frac{\partial(e^{\beta t}R(\mathbf{r},t))}{\partial t}=e^{\beta t}Q(\mathbf{r},t). \tag{23}$$

Equations of this form can be discretized using the time-staggered scheme

$$\frac{e^{\beta(t+\Delta t)}R(\mathbf{r},t+\Delta t)-e^{\beta t}R(\mathbf{r},t)}{\Delta t}=e^{\beta(t+\Delta t/2)}Q(\mathbf{r},t+\Delta t/2), \tag{24}$$

and the equivalent form

$$R(\mathbf{r},t+\Delta t)=e^{-\beta\Delta t/2}(e^{-\beta\Delta t/2}R(\mathbf{r},t)+\Delta t Q(\mathbf{r},t+\Delta t/2)). \tag{25}$$

To obtain the final k-space scheme including PML and relaxation absorption, Eq. (25) is applied directly to Eqs.

(19). The spatial derivatives are replaced by the k-space operators (8), and the particle velocity variables u_x and u_y are evaluated on staggered spatial and temporal grids, as in the lossless algorithm of Eq. (10). The state variables $S_i^{(\cdot)}$ are evaluated using a staggered-time scheme. The final discrete field equations, written in a form suitable for direct numerical implementation, are

$$
\begin{aligned}
u_x(\mathbf{r}_1,t^+) &= e^{-\alpha_x(\mathbf{r}_1)\Delta t/2}\left[e^{-\alpha_x(\mathbf{r}_1)\Delta t/2}u_x(\mathbf{r}_1,t^-) - \frac{\Delta t}{\rho(\mathbf{r}_1)}\left(\frac{\partial(p_x(\mathbf{r},t)+p_y(\mathbf{r},t))}{\partial^{(c_0\Delta t)^+}x}\right)\right],\\
u_y(\mathbf{r}_2,t^+) &= e^{-\alpha_y(\mathbf{r}_2)\Delta t/2}\left[e^{-\alpha_y(\mathbf{r}_2)\Delta t/2}u_y(\mathbf{r}_2,t^-) - \frac{\Delta t}{\rho(\mathbf{r}_2)}\left(\frac{\partial(p_x(\mathbf{r},t)+p_y(\mathbf{r},t))}{\partial^{(c_0\Delta t)^+}y}\right)\right],\\
p_x(\mathbf{r},t+\Delta t) &= e^{-\mu_x(\mathbf{r})\Delta t/2}\left[e^{-\mu_x(\mathbf{r})\Delta t/2}p_x(\mathbf{r},t) - \frac{\Delta t}{\kappa_\infty(\mathbf{r})}\times\left(\frac{\partial u_x(\mathbf{r}_1,t^+)}{\partial^{(c_0\Delta t)^-}x} - \sum_{i=1}^{N}\nu_i^x(\mathbf{r})\,S_i^x(\mathbf{r},t^+)\right)\right],\\
p_y(\mathbf{r},t+\Delta t) &= e^{-\mu_y(\mathbf{r})\Delta t/2}\left[e^{-\mu_y(\mathbf{r})\Delta t/2}p_y(\mathbf{r},t) - \frac{\Delta t}{\kappa_\infty(\mathbf{r})}\times\left(\frac{\partial u_y(\mathbf{r}_2,t^+)}{\partial^{(c_0\Delta t)^-}y} - \sum_{i=1}^{N}\nu_i^y(\mathbf{r})\,S_i^y(\mathbf{r},t^+)\right)\right],\\
S_i^x(\mathbf{r},t^+) &= e^{-\Delta t/[2\tau_i(\mathbf{r})]}\left[e^{-\Delta t/[2\tau_i(\mathbf{r})]}S_i^x(\mathbf{r},t^-) + \Delta t\frac{p_x(\mathbf{r},t)}{\tau_i(\mathbf{r})}\right],\\
S_i^y(\mathbf{r},t^+) &= e^{-\Delta t/[2\tau_i(\mathbf{r})]}\left[e^{-\Delta t/[2\tau_i(\mathbf{r})]}S_i^y(\mathbf{r},t^-) + \Delta t\frac{p_y(\mathbf{r},t)}{\tau_i(\mathbf{r})}\right],
\end{aligned}
\tag{26}
$$

where the quantities μ and ν are defined by Eqs. (20) and (21), respectively.

This scheme provides spatial derivatives with spectral accuracy, temporal iteration that is exact for a homogeneous, lossless medium, and additional corrections that allow stable computations to be made in the presence of large absorption coefficients. The incorporation of relaxation processes allows simulation of realistic absorption in tissue, while use of the PML allows accurate computations to be carried out using small grid sizes. As shown below, the combination of these characteristics results in a powerful and flexible method for computation of ultrasonic propagation over long distances in inhomogeneous media such as soft tissues.

III. NUMERICAL METHODS

Numerical implementation of the present k-space method was accomplished using Eq. (26) directly. The k-space operators of Eqs. (8) were evaluated using two-dimensional discrete Fourier transforms, implemented using a fast Fourier transform (FFT) method.[18]

Initial conditions were chosen to specify a pulsatile incident plane wave with sinusoidal time variation and a Gaussian envelope. Boundary conditions were given by the perfectly matched layer (PML) on all sides of the grid. The absorption parameters α_x and α_y were tapered within the PMLs using formulas of the form[19]

$$\alpha_x = A\frac{c_0}{\Delta x}\left(\frac{x-x_0}{x_{\max}-x_0}\right)^4, \tag{27}$$

where x_0 is the coordinate at the inner edge of the PML, $x_{\max}$ is the coordinate at the outer edge of the grid, and A is the maximum absorption per cell, in nepers, within the PML. A PML thickness of 9 grid points, together with a maximum PML absorption A of 4 nepers per cell, were found to be sufficient to reduce boundary reflection and transmission coefficients below -90 dB for normally incident waves.

Relaxation-process absorption was implemented using two relaxation processes. The parameters κ_i and τ_i were chosen to approximate a linear dependence of absorption on frequency over the pulse bandwidth, using the formula for frequency-dependent absorption given in Ref. 8. The relaxation times chosen were

$$\tau_1 = \frac{1}{5\,f_{\max}}, \quad \tau_2 = \frac{2}{f_{\max}}, \tag{28}$$

where $f_{\max}$ is the nominal maximum frequency of interest. For a maximum frequency of 5 MHz, these are $\tau_1 = 40$ ns and $\tau_2 = 400$ ns. Given this choice of relaxation times, an absorption frequency dependence of 0.5 dB/cm/MHz is best approximated (in a least-squares sense) for the frequency range $0 < f < 5$ MHz by the compressibility coefficients $\kappa_1 = 0.004\,749\,\kappa_\infty$ and $\kappa_2 = 0.004\,562\,\kappa_\infty$.

Benchmark computations analogous to those described in Ref. 6 were carried out to test the accuracy and stability of the present k-space method. As in Ref. 6, time-domain scattered fields for cylindrical test objects were computed and quantitatively compared to an exact solution[20] using an L^2 error metric.[21] The primary test object was, as in Ref. 6, a cylinder with radius 2.0 mm and acoustic properties of human fat ($c = 1.478$ mm/μs, $\rho = 0.950$ g/cm^3)[11] in a background medium with acoustic properties of water at body temperature ($c = 1.524$ mm/μs, $\rho = 0.993$ g/cm^3). The incident pulse was a plane-wave with Gaussian temporal characteristics, a center frequency of 2.5 MHz, a temporal Gaussian parameter $\sigma = 0.25\,\mu$s, which corresponds to a -6-dB bandwidth of 1.5 MHz, and a central starting position of $x = -4.5$ mm at time zero. Time histories of the total pressure field were recorded, at 128 equally spaced ''measurement'' points spanning a circle of radius 2.5 mm concentric to the cylinder, using the interpolation method described in Ref. 6. Another benchmark employed the same configuration except that the cylinder had the density and sound speed of human bone ($c = 3.540$ mm/μs, $\rho = 1.990$ g/cm^3).[11]

In some cases, model media were smoothed before the computation to reduce errors associated with aliasing caused by discontinuities. Smoothing was applied by filtering analytic Fourier transforms of the inhomogeneities considered using the half-band spatial-frequency filter described in Ref. 6. This filter was found to give the most satisfactory results

when applied to the quantities $\kappa_\infty(\mathbf{r})$ and $\rho(\mathbf{r})^{-\beta}$, where β is a small coefficient. The accuracy of computations was found not to depend strongly on the value of β employed; the value $\beta = 1/6$ was used in the computations reported here.

A specific test of the smoothing method was implemented by computing scattering from a point (wire) scatterer with dimensions less than the grid resolution. The test object employed in this case was a point-like scatterer with acoustic properties of human bone ($c = 3540$ m/s, $\rho = 1.990$ g/cm^3) and a radius of 20 μm. Computations were performed with a spatial step of $\Delta x = 0.0833$ mm (four points per nominal minimum wavelength of 0.333 mm) and a Courant–Friedrichs–Lewy number (CFL$\equiv c_0 \Delta t/\Delta x$) of 0.1. For a k-space computation with smoothing, the model medium was obtained by the spatial-frequency filtering procedure described above applied to the analytic Fourier transform of the subresolution scatterer. For comparison, a computation using a discrete single-grid-point scatterer was also carried out. In this case, the scatterer sound speed and density were decreased so that the compressibility contrast γ_κ and the density contrast γ_ρ decreased in proportion to the relative increase in area, which corresponds (for a scatterer of dimensions much smaller than the wavelength) to constant scattering strength.[20] For a scatterer area of 0.0833×0.0833 mm^2 (one grid point), this corresponds to a sound speed of 1.5897 mm/μs and a density of 1.0921 g/cm^3. Computational configurations were the same as for the 2.0-mm radius cylinder benchmarks, except that scattered fields (determined by subtracting the computed incident field in the absence of the scatterer) instead of total fields were compared to the corresponding exact solutions.

Implementation of relaxation absorption was tested in the k-space method by computing propagation of a plane-wave pulse in an absorbing medium. The pulse employed was a Gaussian-modulated sinusoid with a temporal Gaussian parameter of 0.25 μs. Propagation of this pulse was computed for a medium with absorption of 0.5 dB/cm/MHz (parameters τ_0, τ_1, κ_0, and κ_1 as given above), using a spatial step of $\Delta x = 0.0833$ mm (4 points per nominal minimum wavelength). Waveforms were recorded at virtual measurement locations separated by 5 mm along the direction of propagation. The attenuation for the computed propagation was determined numerically as a function of frequency from the ratio of the two-pulse spectra, while the phase speed was determined numerically from the frequency-dependent phase change between the two pulses. These computed values were then compared with theoretical values, given by formulas available in Ref. 8.

An example computation, illustrating the performance of the present k-space method for large-scale problems relevant to ultrasonic imaging, was undertaken using a model tissue-mimicking phantom. This phantom is a 48-mm-diameter cylinder ($c = 1.567$ mm/μs, $\rho = 1.040$ g/cm^3) with two internal 10-mm diameter cylinders ($c = 1.465$ mm/μs, $\rho = 0.0940$ g/cm^3) and three internal 0.2-mm diameter wires ($c = 2.600$ mm/μs, $\rho = 1.120$ g/cm^3) in a background medium with properties of water ($c = 1.509$ mm/μs, $\rho = 0.997$ g/cm^3). The 48-mm cylinder also contained simulated random scatterers, implemented by applying a Gaussian random perturbation with rms amplitude 1% to the compressibility. The internal 10-mm cylinders and wires were not perturbed in this manner. The incident plane wave had a center frequency of 2.5 MHz, a -6-dB bandwidth of 1.7 MHz, and a propagation direction of 37° from the x axis, and was apodized using the window

$$A(\xi) = \{\mathrm{erf}[5(\xi + w_1/2 + w_2/2)/w_2] - \mathrm{erf}[5(\xi - w_1/2 - w_2/2)/w_2]\}/2, \quad (29)$$

where erf is the error function and ξ is an azimuthal distance along the initial wavefront. This window approximates a spatially limited plane wave of the width w_1 with tapered ends of width w_2. The window parameters employed for this example were $w_1 = 48$ mm (the diameter of the phantom) and $w_2 = 6$ mm. The grid size employed was 768×768 with a spatial step of 0.12 mm and a time step of 0.02 μs (CFL $= 0.25$ based on the background sound speed).

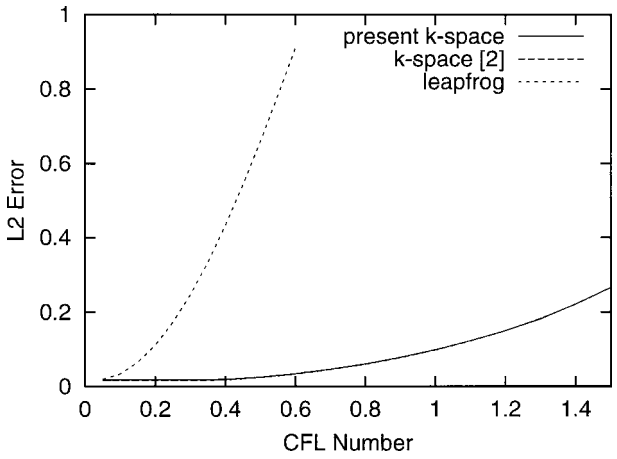

FIG. 3. Time-domain comparison of accuracy for the k-space and leapfrog pseudospectral methods as a function of CFL number. Each test used the "fat" cylinder of 2.0 mm radius and a spatial step size of 4 points per minimum wavelength.

IV. NUMERICAL RESULTS

The previous k-space method based on the second-order wave equation[2,5,6] has been shown in Refs. 6 and 7 to provide high accuracy for weakly scattering media. Spectral evaluation of spatial derivatives provides much higher accuracy than typical finite-difference methods for comparable spatial steps. The $k-t$ space iteration scheme of Ref. 2 provides unconditionally stable computations for media with $c(\mathbf{r}) \leqslant c_0$ (Ref. 6) and allows large time steps to be employed while maintaining accuracy higher than comparable pseudospectral methods.[6,7]

Not surprisingly, the k-space method described here, which is based on coupled first-order wave propagation equations, has numerical properties very similar to those of the original k-space method. Figures 3 and 4, similar to Figs. 2 and 3 of Ref. 6, show the time-domain L^2 error as a function of the spatial and temporal sampling parameters. Figure 3, which shows computations made using the 2.0-mm-radius "fat" cylinder described above and a spatial step size of 4 points per minimum wavelength, show that the present k-space method exhibits temporal accuracy almost identical

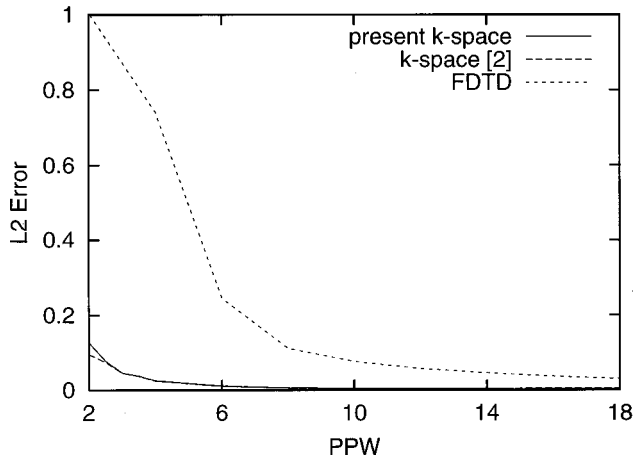

FIG. 4. Time-domain comparison of accuracy for the k-space and 2–4 finite-difference time-domain methods as a function of the spatial step size in points per minimum wavelength (PPW). Each test used the fat cylinder of 2.0-mm radius. CFL numbers were 0.5 for the k-space methods and 0.25 for the finite-difference time-domain method.

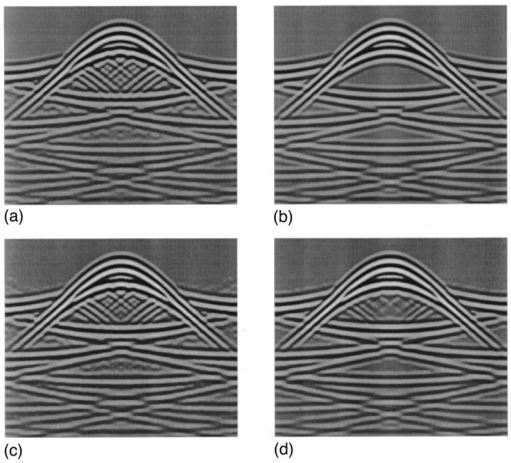

FIG. 5. Computed pressure waveforms at a receiver radius of 2.5 mm for a ''bone'' cylinder of radius 2.0 mm and a pulse center frequency of 2.5 MHz. The acoustic pressure is shown on a bipolar logarithmic scale with a 60-dB dynamic range. The horizontal range of each plot is 360°, covering the entire measurement circle starting with angle 0 (forward propagation). The vertical range of each panel corresponds to a temporal duration of 9 μs, with $t=0$ at the top of each plot. (a) Unsmoothed object; present k-space method, L^2 error 0.2292. (b) Smoothed object; present k-space method, L^2 error 0.0263. (c) Unsmoothed object; previous k-space method,[6] L^2 error 0.3060. (d) Smoothed object; previous k-space method,[6] L^2 error 0.2687.

to the k-space method of Ref. 6. Figure 3 also shows that both k-space methods provide much higher accuracy than a comparable pseudospectral method employing a leapfrog propagator (described in Ref. 6). Similar gains in accuracy have been obtained relative to a more sophisticated pseudospectral method incorporating fourth-order Adams–Bashforth iteration.[7] All three methods provide equivalent results for very small time steps (CFL numbers less than about 0.1), but the k-space methods maintain high accuracy up to a CFL number of about 0.4. In contrast, the leapfrog pseudospectral method rapidly increases in error for CFL numbers above 0.1.

The spatial accuracy of the present k-space method is compared to the previous k-space method[6] and to a 2–4 finite-difference method[11] in Fig. 4. Time-domain L^2 errors are shown, for the 2.0-mm-radius ''fat'' cylinder, as a function of the spatial step size (in points per wavelength, based on a nominal minimum wavelength of 0.333 mm). For these computations, the CFL number of the k-space computations was held constant at 0.5, consistent with the CFL-accuracy relationship shown in Fig. 3, while the CFL number of the finite-difference computations was held at an optimal value of 0.25.[21,22] Again, the present k-space method yields accuracy almost identical to that of the previous k-space method of Ref. 6. All three methods achieve high accuracy for finer grid spacings; however, the k-space methods achieve higher accuracy for much larger spatial step sizes. The L^2 error drops below 0.05 for k-space computations employing only 3 points per minimum wavelength, while achievement of the same accuracy criterion requires 14 points per minimum wavelength for the finite-difference computations.

Although the present k-space method and that of Ref. 6 yield nearly equivalent results for the benchmark case illustrated in Figs. 3 and 4, the use of coupled first-order equations in the present k-space method can provide greater accuracy for strongly scattering media. These advantages are illustrated using a benchmark computation for a 2-mm ''bone'' cylinder, introduced in Ref. 6. Since computations became unstable in this case for CFL numbers above about 0.2 [comparable to the theoretical upper stability limit of 0.2833 given by Eq. (12)], a CFL number of 0.1 was employed for the benchmark. Simulated waveforms obtained using the present k-space method and the previous k-space method of Ref. 6 are presented in Fig. 5 (computations carried out using the method of Ref. 6 were identical to those described in Ref. 6 except that the CFL number was reduced to 0.1). Both before and after smoothing of the model medium, the present k-space method achieves much higher accuracy than the previous method (L^2 error, relative to an exact series solution, was 0.2292 vs 0.3060 before smoothing, 0.0263 vs 0.2687 after smoothing). In addition, artifacts are greatly reduced in the computations employing the present k-space method. The waveforms obtained using the present k-space method with smoothing [panel (b)] are visually identical to those obtained from the exact series solution, shown in Ref. 6.

Further demonstration of the effectiveness of the present k-space algorithm, in conjunction with the smoothing methods used here, is given by Fig. 6. This figure illustrates numerical results for scattering from a bone-mimicking cylinder of sub-grid-resolution size (radius 0.02 mm [20 μm] compared to a spatial step of $\Delta x = 0.0833$ mm). The model medium, obtained by smoothing this subresolution cylinder using the methods described above, results in a scattered amplitude that is nearly identical to the exact solution. The corresponding discrete computation, which attempts to represent the subresolution scatterer using a single pixel with adjusted acoustic parameters, accurately obtains the waveform shape and delay, but incorrectly predicts the angle-dependent scattered amplitude. The accurate scattering computed for the half-band filtered medium indicates that the present k-space method, with smoothing of the kind used here, can account for structures with dimensions smaller than

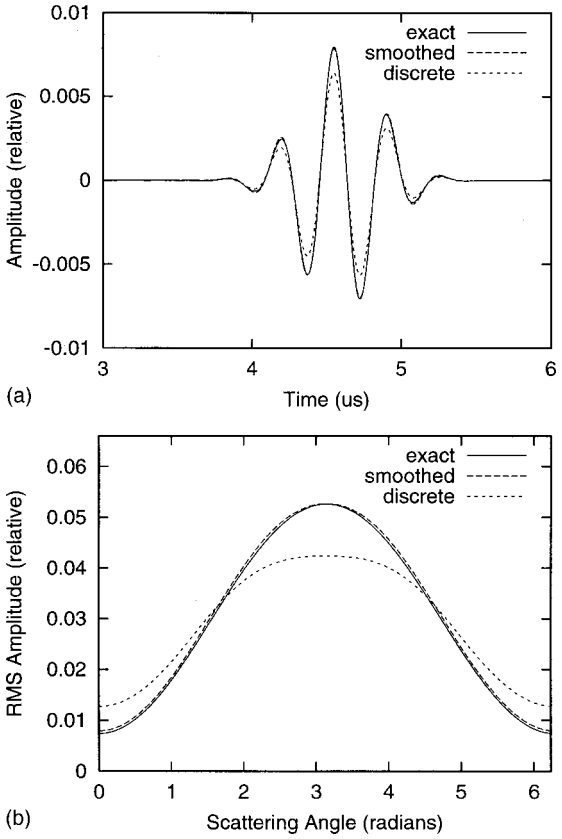

FIG. 6. Simulated scattering from a point (wire) scatter with radius 20 μm and acoustic properties of human bone. Each plot shows results for an exact series solution, a *k*-space solution using a half-band filtered representation of the subresolution scatterer (''smoothed''), and a single-pixel representation with equal scattering strength. (a) Backscattered signals. (b) The rms waveform amplitudes.

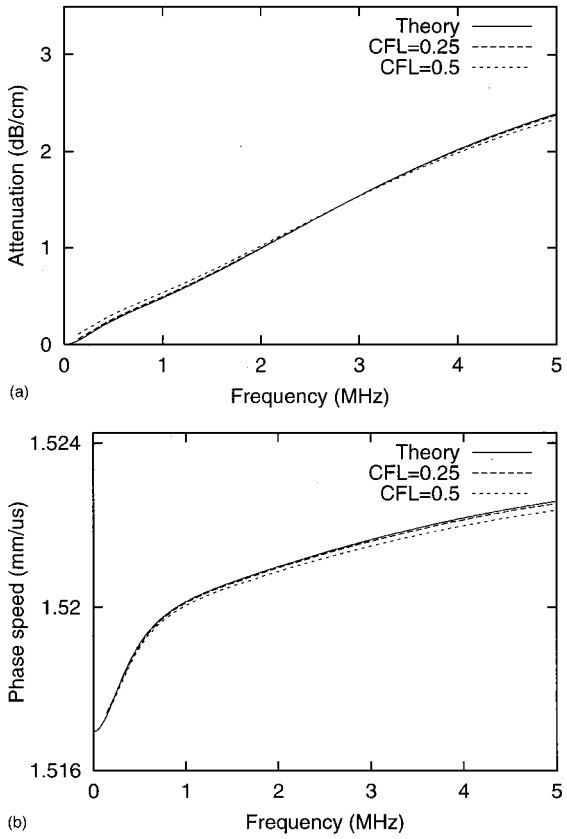

FIG. 7. Attenuation and phase speed for propagation of a pulse in a medium with two relaxation processes. Each panel shows theoretical values (Ref. 8) and values obtained using the present *k*-space method for two values of the CFL number. (a) Frequency-dependent attenuation. (b) Frequency-dependent phase speed.

the spatial step employed. Given sufficiently fine spatial sampling (4 points per minimum wavelength), scattering can be accurately computed from subgrid-sized structures located at arbitrary positions.

Results of the numerical test of relaxation absorption are illustrated in Fig. 7. Panel (a) shows theoretical and simulated attenuation values, while panel (b) shows theoretical and simulated values of the phase speed. The simulations are for two sizes of the time step corresponding to CFL$=0.25$ and CFL$=0.5$. The case with a smaller time step (CFL $=0.25$) agrees very well with the theory, while the case with a larger time step (CFL$=0.5$, as employed in the soft-tissue benchmark computations described above) shows good qualitative agreement. These results illustrate that the present *k*-space method with relaxation absorption can realistically simulate attenuation caused by soft tissues even for relatively coarse time steps.

Numerical results for the tissue-mimicking phantom example, described in the previous section, are illustrated in Fig. 8. This figure shows four snapshots of the spatially limited plane wave propagating through the phantom, causing coherent reflection from boundaries and wires as well as incoherent scattering from the random structure within the background cylinder. Notable is that smoothing of the medium has reduced any ringing artifacts to a level far below the low-level random scattering within the cylinder. Also notable is that the use of PML absorbing boundary conditions allows the computation shown to be performed efficiently (4063 CPU s on a 650-MHz Athlon processor for a simulation of duration 360 μs on a 768×768 grid). A hypothetical computation without absorbing boundaries, in which the grid size would be expanded to eliminate wraparound error within the region shown in Fig. 8, would require a grid size of approximately 4600×4600 points, resulting in a 35-fold increase in storage and computation time requirements.

V. DISCUSSION

The starting point for the *k*-space method introduced here is the previous *k*-space method based on the second-order wave equation.[2,6] Thus, a brief discussion of similarities and differences between these two methods is appropriate.

The two methods show identical accuracy for homogeneous media, since they are mathematically identical in this case. For weakly inhomogeneous media, both methods have similar performance in accuracy and stability. However, for stronger inhomogeneities such as the bone-mimicking cylinder benchmark described here, the two *k*-space methods differ significantly. The present method, based on the coupled first-order wave propagation equations, achieves much higher accuracy, although numerical evidence suggests that the present method has a lower stability threshold than the

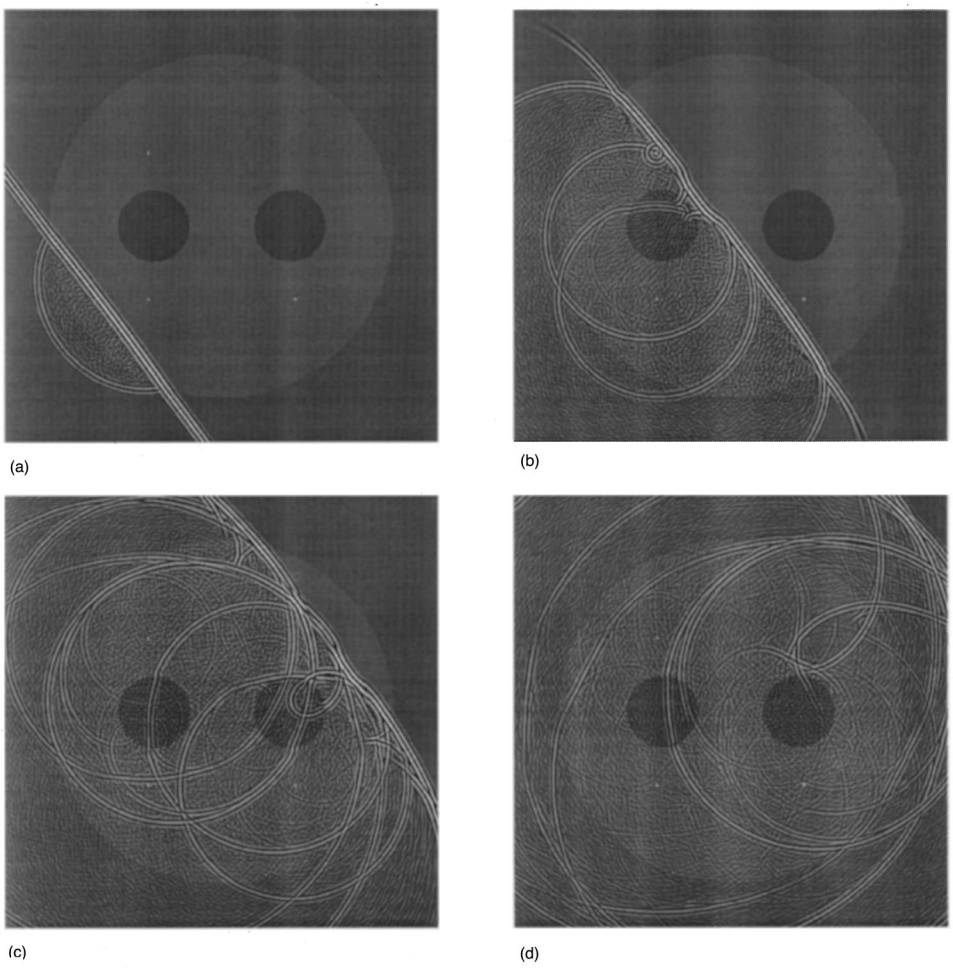

FIG. 8. Computed pressure fields for a 48-mm diameter tissue-mimicking phantom. Panels (a)–(d) show the total acoustic pressure at intervals of 12 μs, superimposed on an image of the phantom. The area shown in each panel is 61×61 mm. Wave fields are plotted using a bipolar logarithmic scale with a dynamic range of 60 dB.

method of Ref. 6. The increased accuracy of the present k-space method for high-contrast media, relative to previous k-space methods based on second-order wave equations,[6] occurs for several likely reasons. Since the k-space method for coupled first-order propagation equations can be written in a form involving no Fourier transforms of medium properties [Eq. (10)], some aliasing errors may be eliminated. In addition, the coupled first-order equations incorporate the density directly rather than within a derivative term, so that errors associated with inaccuracies in discrete derivatives of the density are also reduced.

The two methods also differ somewhat in computation and storage requirements. The method of Ref. 6 requires computation and storage of only one acoustic variable (the acoustic pressure fluctuation), while the present method requires computation of the pressure fluctuation as well as each vector component of the acoustic particle velocity fluctuation. Thus, for a constant grid size, the present k-space method requires somewhat greater storage and computation time than the method of Ref. 6. However, this difference is offset by the capability of the present k-space method to incorporate PML absorbing boundary conditions. For large computations, the high performance of the PML allows the grid size to be substantially reduced without introduction of wraparound or boundary-reflection errors, so that the present k-space method is often more efficient for practical problems. This advantage is potentially even more important for three-dimensional computations.

The present k-space method can also be compared with pseudospectral methods for coupled first-order propagation equations (e.g., Refs. 12, 13, and 17). Although both methods use Fourier transforms to accurately evaluate the spatial first-order derivative, the present k-space method also includes temporal correction terms, which were obtained by factoring the second-order k-space operator of Eq. (7) into the first-order operators of Eq. (8). As a result, the present k-space method utilizes two-dimensional Fourier transforms, while pseudospectral methods employ one-dimensional Fourier transforms for calculation of spatial derivatives. This difference leads to a slight increase in computational requirements associated with Fourier transforms. Typically, pseudospectral methods require eight sets of one-dimensional Fourier transforms per time step, while the present k-space method requires seven two-dimensional Fourier transforms per time step. However, the temporal correction provided by the k-space method eliminates the need for higher-order time schemes such as Adams–Bashforth and Adams–Moulton iteration, so that the k-space method may

provide improved overall efficiency. This advantage occurs in part because the *k*-space method can provide accurate results for larger time steps (higher CFL numbers) than pseudospectral methods employing higher-order temporal iteration.[7]

Another advantage of the present *k*-space method is the close analogy between this method and the standard finite-difference time-domain method of Ref. 16. The present *k*-space method is algorithmically identical to the method of Ref. 16 except that second-order-accurate spatial derivatives have been replaced by the *k*-space operator of Eq. (8), which provides spectral accuracy in space, exact temporal iteration for homogeneous media, and high accuracy for general media. This close analogy has allowed relaxation absorption and PMLs, previously adapated to the corresponding finite-difference method,[9] to be straightforwardly incorporated into the present *k*-space method. The analogy allows great improvements in the performance and accuracy of existing finite-difference codes employing algorithms similar to those of Refs. 9 and 16 by the straightforward replacement of finite-difference spatial derivatives with the *k*-space operators of Eq. (8).

VI. CONCLUSIONS

The present *k*-space method, which numerically solves the coupled first-order differential equations for wave propagation in inhomogeneous fluid media, has been shown to hold a number of advantages for large-scale simulation of ultrasound–tissue interaction.

The method maintains the major advantages of previous *k*-space methods;[6] like those, the present method is spectrally accurate in space, temporally exact for homogeneous media, and highly accurate for modest medium variations. Furthermore, the form of the present method has allowed it to be extended with PML absorbing boundary conditions, relaxation absorption, and an effective approach to smoothing discontinuous scattering media. Since the present method can be interpreted as a finite-difference method with correction terms, existing finite-difference codes may be easily modified to take advantage of the accuracy available from the *k*-space method.

Numerical examples presented here have shown that the present *k*-space method has remarkable accuracy and stability characteristics, similar to previous *k*-space methods,[6] for computations involving weakly scattering media. The method, together with the smoothing approach presented here, provides higher accuracy for strongly scattering media. Since *k*-space methods allow highly accurate results to be obtained using coarse spatial and temporal sampling, the present *k*-space method, with the incorporation of PML absorbing boundary conditions and relaxation absorption, is particularly well-suited to realistic large-scale simulations for applications including ultrasonic imaging studies.

ACKNOWLEDGMENTS

This research was funded by NIH Grants Nos. HL 50855, CA 74050, and CA 81688, US Army Grant DAMD-17-98-1-8141, DARPA Grant N00014-96-0749, and the University of Rochester Diagnostic Ultrasound Research Laboratory Industrial Associates.

[1] N. N. Bojarski, ''The *k*-space formulation of the scattering problem in the time domain,'' J. Acoust. Soc. Am. **72**, 570–584 (1982).

[2] N. N. Bojarski, ''The *k*-space formulation of the scattering problem in the time domain: An improved single propagator formulation,'' J. Acoust. Soc. Am. **77**, 826–831 (1985).

[3] B. Compani-Tabrizi, ''*K*-space formulation of the absorptive full fluid elastic scalar wave equation in the time domain,'' J. Acoust. Soc. Am. **79**, 901–905 (1986).

[4] S. Finette, ''Computational methods for simulating ultrasound scattering in soft tissue,'' IEEE Trans. Ultrason. Ferroelectr. Freq. Control **34**, 283–292 (1987).

[5] S. Pourjavid and O. J. Tretiak, ''Numerical solution of the direct scattering problem through the transformed acoustical wave equation,'' J. Acoust. Soc. Am. **91**, 639–645 (1992).

[6] T. D. Mast, L. P. Souriau, D.-L. Liu, M. Tabei, A. I. Nachman, and R. C. Waag, ''A *k*-space method for large-scale models of wave propagation in tissue,'' IEEE Trans. Ultrason. Ferroelectr. Freq. Control **48**, 341–354 (2001).

[7] J. C. Mould, G. L. Wojcik, L. M. Carcione, M. Tabei, T. D. Mast, and R. C. Waag, ''Validation of FFT-based algorithms for large-scale modeling of wave propagation in tissue,'' Proc. IEEE Ultrason. Symp. 1999, **2**, 1551–1556 (1999).

[8] A. I. Nachman, J. F. Smith, and R. C. Waag, ''An equation for acoustic propagation in inhomogeneous media with relaxation losses,'' J. Acoust. Soc. Am. **88**, 1584–1595 (1990).

[9] X. Yuan, D. Borup, J. Wiskin, M. Berggren, and S. A. Johnson, ''Simulation of acoustic wave propagation in dispersive media with relaxation losses by using FDTD method with PML absorbing boundary condition,'' IEEE Trans. Ultrason. Ferroelectr. Freq. Control **46**, 14–23 (1999).

[10] A. D. Pierce, *Acoustics: An Introduction to its Physical Principles and Applications*, 2nd ed. (Acoustical Society of America, Woodbury, NY, 1989), Chap. 1.

[11] T. D. Mast, L. M. Hinkelman, M. J. Orr, V. W. Sparrow, and R. C. Waag, ''Simulation of ultrasonic pulse propagation through the abdominal wall,'' J. Acoust. Soc. Am. **102**, 1177–1190 (1998).

[12] B. Fornberg, *A Practical Guide to Pseudospectral Methods* (Cambridge University Press, Cambridge, 1996).

[13] G. Wojcik, B. Fornberg, R. Waag, L. Carcione, J. Mould, L. Nikodym, and T. Driscoll, ''Pseudospectral methods for large-scale bioacoustic models,'' Proc. IEEE Ultrason. Symp. 1997, **2**, 1501–1506 (1997).

[14] B. Fornberg and G. B. Whitham, ''A numerical and theoretical study of certain nonlinear wave phenomena,'' Philos. Trans. R. Soc. London **289**, 373–404 (1978).

[15] Ronald A. Mickens, *Nonstandard Finite Difference Models of Differential Equations* (World Scientific, Singapore, 1994).

[16] K. S. Yee, ''Numerical solution of initial boundary value problems involving Maxwell's equations in isotropic media,'' IEEE Trans. Antennas Propag. **14**, 302–307 (1966).

[17] H.-W. Chen, ''Staggered-grid pseudospectral viscoacoustic wave field simulation in two-dimensional media,'' J. Acoust. Soc. Am. **100**, 120–131 (1996).

[18] M. Frigo and S. G. Johnson, ''FFTW: An adaptive software architecture for the FFT,'' Proc. ICASSP, **3**, 1381–1384 (1998).

[19] J. Mould, D. K. Vaughan, and L. Carcione, SPECTRALFLEX *User's Manual* (Weidlinger Associates, Los Altos, CA, 1999).

[20] P. M. Morse and K. U. Ingard, *Theoretical Acoustics* (McGraw-Hill, New York, 1968), Chap. 8.

[21] R. L. Burden, J. D. Faires, and A. C. Reynolds, *Numerical Analysis* (Prindle, Weber, and Schmidt, Boston, 1978), Chap. 8.

[22] E. Turkel, ''On the practical use of high-order methods for hyperbolic systems,'' J. Comput. Phys. **35**, 319–340 (1980).